



Interface reinforced 2D/2D heterostructure of Cu-Co oxides/FeCo hydroxides as monolithic multifunctional catalysts for rechargeable/flexible zinc-air batteries and self-powered water splitting

Xuhuan Yang^a, Zining Zhou^a, Yueyuan Zou^a, Jiaqi Kuang^a, Dewei Ye^a, Shengsen Zhang^{a,b,*}, Qiongzhi Gao^{a,b}, Siyuan Yang^{a,b}, Xin Cai^{a,b,*}, Yueping Fang^{a,b}

^a College of Materials and Energy, South China Agricultural University, Guangzhou, Guangdong 510642, China

^b Guangdong Laboratory for Lingnan Modern Agriculture, South China Agricultural University, Guangzhou, Guangdong 510642, China

ARTICLE INFO

Keywords:

Zin-air batteries
HER/OER/ORR
2D/2D Heterostructure
Bifunctional catalysts
Interfacial coupling

ABSTRACT

Elaborate engineering of heterostructure and composition to regulate the electroactivities remains a pronounced challenge. Herein, a self-supported 2D/2D heterostructure monolith is constructed by interlinked FeCo-hydroxides nanosheets tightly interlacing with aligned $\text{Cu}_{0.76}\text{Co}_{2.24}\text{O}_4$ nanoplates. Due to the well-defined hierarchical nanoarrays and desirable interfacial coupling, the monolithic catalyst can guarantee the rapid charge transfer and mass transport pathways for accelerated surface kinetics, leading to manifestly improved electroactivities and stability toward trifunctional catalysis. Both experimental and theoretical calculations unravel the enriched multimetal active sites for intermediates adsorption and the synergistic interplay of the heterostructure to achieve enhanced catalytic efficiency. Consequently, the heterostructure catalyst contributes to high-performance rechargeable/flexible all-solid-stated Zn-air batteries and water electrolyzer with an ultralow potential of 1.51 V. Moreover, self-powered water splitting system driven by flexible Zn-air batteries delivers a high H_2 generation rate. This cost-effective heterostructure monolith could open an intriguing avenue for advancing all-in-one films toward portable energy conversion/storage.

1. Introduction

The ever-expanding energy demand and environmental concerns have prompted the urgent exploration of renewable energy capture and utilization. Fundamental electrochemical reactions, such as the oxygen evolution reaction (OER) and hydrogen evolution reaction (HER) in overall water splitting for clean H_2 production, and OER/oxygen reduction reaction (ORR) to activate metal-air batteries or fuel cells, *etc.*, markedly impact the energy efficiencies and the power output of these promising energy storage/conversion devices [1–3]. Unfortunately, the sluggish kinetics of OER/ORR/HER on the functional electrodes always cause pronounced overpotentials and unsatisfied operational tolerance, largely caused by the multiphase interfacial reactions associated with intricate electron transfer process. Being capable of high activities, practical stability and economic cost, ideal electrocatalysts are thus extremely desired to speed up the redox kinetics of the electrochemical process [4–6]. Up to now, noble-metal catalysts, *i.e.*, Pt-based and Ru, Ir-based catalysts, still stand as the benchmarks in light of the

effectiveness for catalyzing ORR/HER and OER, respectively. Still, the prohibitive scarcity and deficient long-term durability of those noble-metal catalysts unavoidably hinder the scalable use, let alone their lack of multifunctional activities for several electrocatalytic reactions [7]. Indeed, multifunctional catalysts with the ability to simultaneously boost OER/ORR/HER are even more attractive and valuable. For instance, the crucial air cathode side of zinc-air batteries (ZABs) requires oxygen catalysts possessing adorable OER/ORR bifunctionality [8]. The intelligent adoption of multifunctional electrocatalysts will minimize the amount/cost and tedious mixing of single-functional catalysts, but also appreciably simplify the structural design of the electrode/battery [9,10]. Yet, seeking non-precious metal-based electrocatalysts with high cost-efficiency, working stability and superb multifunctionality remains a tough challenge [11].

Over the past decade, tremendous attempts have been made on exploiting efficient precious metal-free electrocatalysts, such as earth-abundant transition metal-based compounds (perovskites, hydroxides, nitrides, phosphide, sulfides and carbides), and especially their

* Correspondence to: College of Materials and Energy, South China Agricultural University, China.

E-mail addresses: zhangss@scau.edu.cn (S. Zhang), caixin2015@scau.edu.cn (X. Cai).

<https://doi.org/10.1016/j.apcatb.2022.122332>

Received 10 June 2022; Received in revised form 26 November 2022; Accepted 26 December 2022

Available online 28 December 2022

0926-3373/© 2022 Elsevier B.V. All rights reserved.

composites incorporating heteroatoms-doped carbon materials [12–17]. In virtue of the natural abundance, mixed valences for appealing electroactivities, redox stability and ecofriendliness, spinel bimetallic oxides ($A_xB_{3-x}O_4$, BMOs)-based catalysts have intrigued continuous attention among the diverse alternative electrocatalysts [18–21]. Strategies of mixed-valence metal ions or secondary metal (e.g. Ni, Mn, Fe) substitution, are found to be quite feasible to improve the intrinsic activities and electrochemical stability of BMO catalysts via introducing useful oxygen vacancies and the electronic modulation of the active metal centers [22,23]. In addition to the phase/composition and stoichiometric adjustment, previous investigations unravel that heterogeneous nanoarchitecture and surface/interface engineering are equally significant [24–26]. Such synergistic approaches have several superiorities: (i) help to expose plentiful electroactive sites and mass transfer channels so as to lower the energy barriers for the adsorption/desorption of the reaction intermediates; (ii) promote the interfacial contact area and the electrolyte penetration; (iii) shorten the charge transport pathways, thereby compensating for the limited electronic conductivity of BMOs, and ultimately enhancing the actual electrocatalytic kinetics of the catalysts. For example, core/shell-structured $NiCo_2O_4$ nanowires@ $NiMn$ LDHs afforded a remarkably lowered OER overpotential of 255 mV at 10 mA cm^{-2} [27]. Zn^{2+} -coordinated $Ni_{1-x}Co_xO_4$ nanoparticles were anchored to N-doped carbon nanotubes (CNTs), which yields optimized physical pore structure and more activated Co sites by zinc defects accounting for improved ORR and OER activities [28]. Nevertheless, the systematic design/regulation of BMOs-based catalysts is not easy, with respect to their particle size, morphology, metal distribution and interfacial properties to achieve optimal electrocatalytic efficiency.

Interestingly, transition metal based-two dimensional (2D) nanomaterials show enormous potential in various catalysis and energy-related fields owing to large exposed specific area, tunable size/composition distribution and rich redox active sites [29,30]. Taking advantages of interfacial electronic coupling, rational heterostructure built from 2D nanostructures can be a potential solution to further improve the electrochemistry of the catalysts [31,32]. Heterostructured $NiFe_2O_4/FeNi_2S_4$ nanosheets developed by Zhang *et al.* set a good example. By synthetically tuning the interfaces over $FeNi_2S_4$ nanoparticles-decorated $NiFe_2O_4$ nanosheets, the catalyst gained increased binding energy with the oxygenated intermediates to accelerate the OER/ORR kinetics even in neutral aqueous electrolyte [33]. However, the overall OER/ORR/HER activities of most existing BMO-based catalysts still can't compete with those of optimized noble-metal catalysts and state-of-the-art atomically dispersed M-N_x-C (M=Co, Fe) catalysts [34]. More notably, the vast majority of developed electrocatalysts are in powder form, and generally adhered/pressed to extra current collectors by slurry coating/spraying using polymeric binders. The inert binders and other conductive additives inevitably dilute the utilization efficiency of the electrocatalysts, as well as increases the interfacial contact resistance of the air electrodes [35,36]. Also, the weakly bonded powder catalysts are prone to fall off from the substrate when the electrode endures flooding and mechanical distortions upon cycling. In contrast, binder-free (self-supported) electrocatalysts are of particular interest, as they exhibit a high integration of the necessary components to make full use of the active substances [37]. These integrated binder-free electrocatalysts are often established by either directly grown on porous conductive substrates or bottom-up nanoassembly of suitable building blocks, enabling the construction of mechanically robust and catalytic film electrodes, which manifest unparalleled advantages in realizing flexible, bendable, and deformable energy devices for portable powers and smart/wearable electronics [38–40]. Thus far, both 2D/2D heterostructured catalysts with self-supporting nature and BMOs-based electrocatalysts with multifunctional ORR/OER/HER activities are rarely reported and deserve further efforts.

Inspired by above concerns, we crafted an *in situ* coupled 2D/2D

heterostructure of Cu-Co bimetal oxides-based monolith (denoted as NF/CCO/FCH) as integrated trifunctional electrocatalysts. Binder-free NF/CCO/FCH was controllably prepared via a facile two-step hydro/solvothermal route, in which vertically aligned nanoarrays of $Cu_{0.76}Co_{2.24}O_4$ (CCO)/FeCo hydroxides (FCH) nanosheets were tightly attached to 3D porous nickel foam (NF). Large triphase boundary area, multiple reactive sites and facilitated charge transfer of the versatile NF/CCO/FCH catalyst can simultaneously boost the essential catalytic kinetics for HER/OER/ORR, originating from the exclusive hetero-nanostructure and the interfacially synergized oxides/hydroxides nanosheets. As a consequence, NF/CCO/FCH realized greatly enhanced multifunctional electroactivities, yielding a low $\eta_{j=10}$ of 175 mV for HER, an overall ΔE of merely 657 mV for OER and ORR that can match the Pt/C+ RuO_2 benchmark. When directly served as the air cathode for both aqueous and flexible ZABs, NF/CCO/FCH contributed to high-performance flexible/rechargeable ZABs with a high energy density of 894.5 Wh kg_{Zn}^{-1} and exceptional cycling stability upon 400 h/1000 cycles. Also, a self-powered overall water splitting cell was constructed with trifunctional NF/CCO/FCH as the sole catalyst, which delivered a high H_2 generation rate.

2. Experimental section

2.1. Synthesis of the heterostructure catalysts

2.1.1. Synthesis of NF/CCO

First, nickel foam (NF, 2 * 2.5 cm^2) was treated with acetone for 5 min and 1 M HCl for 10 min under sonication to remove the surface oxidized layer, followed by ultrasonic clean using deionized water, ethanol, and dried thoroughly before use. Secondly, $Co(NO_3)_2 \cdot 6H_2O$ (1.25 mmol), $Cu(NO_3)_2 \cdot 3H_2O$ (0.6 mmol), and $Co(NH_2)_2$ (4.5 mmol) were uniformly dispersed into 40 mL of deionized water, producing a pink and transparent dispersion via magnetic agitation, which was then transferred into a Teflon-lined stainless autoclave (volume of 50 mL) along with the above-treated NF in it. The system was kept at 120 °C for 8 h-reaction. After being taken out, the obtained monolithic membrane was naturally cooled down to ambient temperature, repeatedly rinsed by deionized water, ethyl alcohol, and endured a thorough vacuum drying. Finally, $Cu_{0.76}Co_{2.24}O_4$ nanosheet arrays on NF (denoted as NF/CCO) was received after calcination at 400 °C (heating rate: 4 °C min^{-1}) for 3 h in air.

2.1.2. Synthesis of NF/CCO/FCH

$Co(NO_3)_2 \cdot 6H_2O$ (3 mmol), $Fe(NO_3)_3 \cdot 9H_2O$ (1 mmol), and $C_6H_{12}N_4$ (0.5 g) were dispersed into methanol (30 mL), experienced magnetical stirring to obtain a uniform solution under ultrasonic treatment. The resulted mixture was shifted into a 50 mL-Teflon-lined stainless steel autoclave (50 mL) with the immersion of the NF/CCO membrane, and heated at 120 °C for 4 h. Afterwards, the reaction system naturally cooled down to ambient temperature. Using deionized water and ethyl alcohol, the as-prepared electrode membrane was rinsed repeatedly, and dried thoroughly in vacuum. The obtained sample was denoted as NF/CCO/FCH. For comparison, the sample fabricated by using the same conditions without CCO was named as FCH (NF/FCH).

2.2. Materials characterization

Scanning electron microscopy (SEM, Zeiss), and Transmission electron microscopy (HR-TEM, Tecnai12, FEI, acceleration voltage of 300 kV) were adopted for the microstructural and morphological analysis of the prepared samples. X-ray diffraction (XRD, Rigaku D/Max 2550) equipped with copper- K_α radiation was utilized to analyze the crystal/phase composition. Inductively Coupled Plasma Optical Emission Spectrometer (ICP-OES, Agilent 730) was employed to determine the metallic content of the catalysts. X-ray photoelectron spectroscopy (XPS, VG ESCALAB250) was carried out for analyzing the chemical states.

2.3. Electrochemical measurements

The electrocatalytic multiactivities of the catalysts were evaluated in a three-electrode system based on CHI electrochemical workstation (760E, China), which consists of the working electrode (1 cm^2), Ag/AgCl reference electrode, and a counter electrode (Pt foil for OER and ORR, or carbon rod for HER tests, respectively). OER, ORR and HER activities of the self-supported catalysts were characterized by linear sweep voltammetry (LSV) polarization curves by the scan rate of 1, 1 and 5 mV s^{-1} in 1 M KOH, respectively. Chronopotentiometry was adopted to characterize the electrochemical stability. According to the cyclic voltammetry (CV) curves occurred in 1 M KOH, electrochemical double layer capacitance (C_{dl}) was obtained to assess the electrochemically active surface area (ECSA), where the voltage window operated at 0.1–0.2 V (vs. Ag/AgCl) under various scan rates ranging from 3 to 15 mV s^{-1} . Electrochemical impedance (EIS) spectra were collected on the CHI650E workstation with 5 mV AC amplitude across the frequency range of 10 kHz–0.1 Hz, and measured at 1.49 V for OER (0.83 V for ORR). Unless specified, all the potentials in this study have been calibrated to potentials versus the reversible hydrogen electrode (RHE) via the equation:

$$E_{\text{RHE}} = E_{(\text{Ag}/\text{AgCl})} + E_{(\text{Ag}/\text{AgCl}, 0.199)}^0 + 0.0591 \text{ pH} \quad (1)$$

Preparation of Pt/C and RuO₂ electrode: RuO₂ (2 mg, Aladdin) or Pt/C (2 mg, 20 wt%, Johnson Matthey Company, HISPEC 3000™) were ultrasonically dispersed in 1 mL ethanol containing 100 μL Nafion solution (0.5 wt%) for 1 h to obtain a homogeneous mixture, respectively. Then the homogeneous dispersion was dripped onto the pretreated NF substrate with the same catalyst loading (2.0 mg cm^{-2}) as reference.

2.4. Fabrication and characterization of aqueous rechargeable ZABs

An aqueous rechargeable zinc-air battery is assembled by a bifunctional oxygen electrode (NF/CCO/FCH, Pt/C+RuO₂, or NF/CCO) as the air cathode, a polished zinc plate (thickness of 300 μm) as the anode, and a mixed alkaline electrolyte of 6 M KOH including 0.2 M Zn(Ac)₂ as additive. For the preparation of Pt/C+RuO₂ electrode, 1 mg of commercial Pt/C and 1 mg of RuO₂ were ultrasonically dispersed for 1 h in 1 mL ethanol containing 100 μL Nafion solution (0.5 wt%) to obtain a homogeneous dispersion, respectively. Then the homogeneous dispersion was dripped onto the pretreated NF substrate to acquire the Pt/C+RuO₂ electrode as a reference under the same conditions. All the electrochemical performances of rechargeable ZABs were measured through CHI760E and a NEWARE battery system (CT-3008), which consumed the ambient air.

2.5. Assembly and characterization of all-solid-stated FZABs

Planar FZABs were assembled by the polymeric gel electrolyte sandwiched between the polished Zn foil and the NF/CCO-based air cathode (without using any other current collector, gas diffusion films or additives). For the preparation of the solid-stated gel electrolyte, 5 mL deionized water was added by 0.25 M ZnO and 11.25 M KOH to produce a mixed dispersion by magnetic agitation. Next, acrylic acid (0.5 g) and N, N'-methylene-bisacrylamide (0.075 g) were dissolved into the above naturally cooled dispersion, and was kept stirring for 5 min, further filtered out the precipitation to form a transparent dispersion. Finally, the transparent dispersion was poured into a petri dish, where, 75 μL 0.3 M K₂S₂O₈ was added to initiate the monomers to polymerize into the gel electrolyte. All the electrochemical performances of FZABs were recorded by CHI 760E and a NEWARE battery system (CT-3008).

2.6. Assembly and characterization of overall water-splitting unit

A homemade overall water splitting cell was assembled by a NF/

CCO/FCH electrode anodic electrode and a NF/CCO/FCH cathodic electrode, respectively. The water splitting activities of NF/CCO/FCH was performed by LSV polarization curves with the scan rate of 1 mV s^{-1} in 1 M KOH. To establish a self-powered water splitting device system, the water splitting cell was directly driven by two in-series connected FZABs for H₂ production. The drainage collection method was adopted to collect the H₂/O₂ bubbles produced by the self-driving overall water splitting device.

3. Results and discussion

3.1. Morphology and structure of the heterostructure catalysts

The preparation process of CCO-based binder-free catalysts are shown in Fig. 1a. Firstly, CuCo hydroxide precursor was *in-situ* and hydrothermally grown onto the pretreated NF substrate, and converted to CCO nanoarrays by subsequent annealing. Fig. 1b demonstrates the interlately stacked CCO nanosheets with a width of 3–5 μm that are vertically aligned on the NF scaffold (Fig. S1a–d, Supporting Information). After the second solvothermal reaction, uniform FCH nanosheets further decorated the thin CCO nanosheets to generate the final NF/CCO/FCH. SEM images of NF/CCO/FCH show that CCO nanosheet arrays are covered by interconnected and ultrathin waved FCH nanosheets (Fig. 1c, d), forming an intersectant 2D/2D heterostructure with mutually 3D cross-linked porous channels, which would promote the penetration of the electrolyte and the diffusion of oxygen (Fig. S2a, b, Supporting Information) [41]. The acquired NF/CCO/FCH monolithic film is free-standing with superb mechanical flexibility/bendability (Fig. S3, Supporting Information), applicable to multifunctional catalysis such as OER, ORR and HER due to the highly conductive NF substrate and the rich electroactive metallic components (Fig. 1a).

X-ray diffraction (XRD) patterns of all the NF-supported catalysts exhibit relatively weak diffraction peaks that were mainly caused by the ultrastrong diffraction signals of the NF substrate (Fig. S4a, b, Fig. S5, Supporting Information). In this regard, the catalyst powder peeled off from NF were ultrasonically collected to accurately analyze the phase composition. The diffraction peaks of CCO are well indexed to the planes of Cu_{0.76}Co_{2.24}O₄ phase (PDF#76–1886) (Fig. 2a, Supporting Information), as further deduced by the stoichiometric composition of Co, Cu and O elements in CCO through ICP-OES (Table S1, Supporting Information) and Energy Disperse Spectroscopy (EDS) analysis (Fig. S6a, b and Table S2, Supporting Information). As for FCH, the diffraction peaks match the planes of typical layered double hydroxides (LDHs) structure [42,43], where the Fe content is estimated to be 0.45 wt% in NF/CCO/FCH according to the EDS analysis (Fig. S7a, b, Table S3, Supporting Information). The results reveal the certain composition of Cu_{0.76}Co_{2.24}O₄ and Fe-doped cobalt hydroxides in CCO/FCH without any obvious impurities.

HR-TEM images identify that the thin nanosheet for individual CCO is composed of ultrafine pea pod-like nanoparticles (diameter of about 7–14 nm) without aggregation (Fig. S8a, b, Supporting Information). This polycrystalline feature of CCO with sufficient grain boundaries is beneficial for the exposure of more reactive sites to improve the inherent electrocatalytic activity of the nanocatalyst [44]. As shown in Fig. 2b and c, the intersectant 2D/2D heterostructure of CCO/FCH further uncovers the rational hybridization of CCO nanosheets (thickness of 10–20 nm) with the epitaxially grown FCH ultrathin nanosheets as well as the close contacts between the two constituents (Fig. S9a, b, Supporting Information). Based on Fig. 2d, the lattice spacings of 0.183 nm, 0.234 nm and 0.243 nm are classified to (331), (222) and (311) crystal planes for spinel Cu_{0.76}Co_{2.24}O₄, while the d-spacing with 0.231 nm belongs to the characteristic (105) plane of hexagonal α -Co(OH)₂ with partial Fe doping, respectively. The hierarchical morphology and well engineered heterointerfaces of CCO/FCH are likely to favor the mass transfer and charge transport across the 2D/2D heterogeneous electrocatalysts [45]. EDS mapping in Fig. 2e illustrates the homogeneous

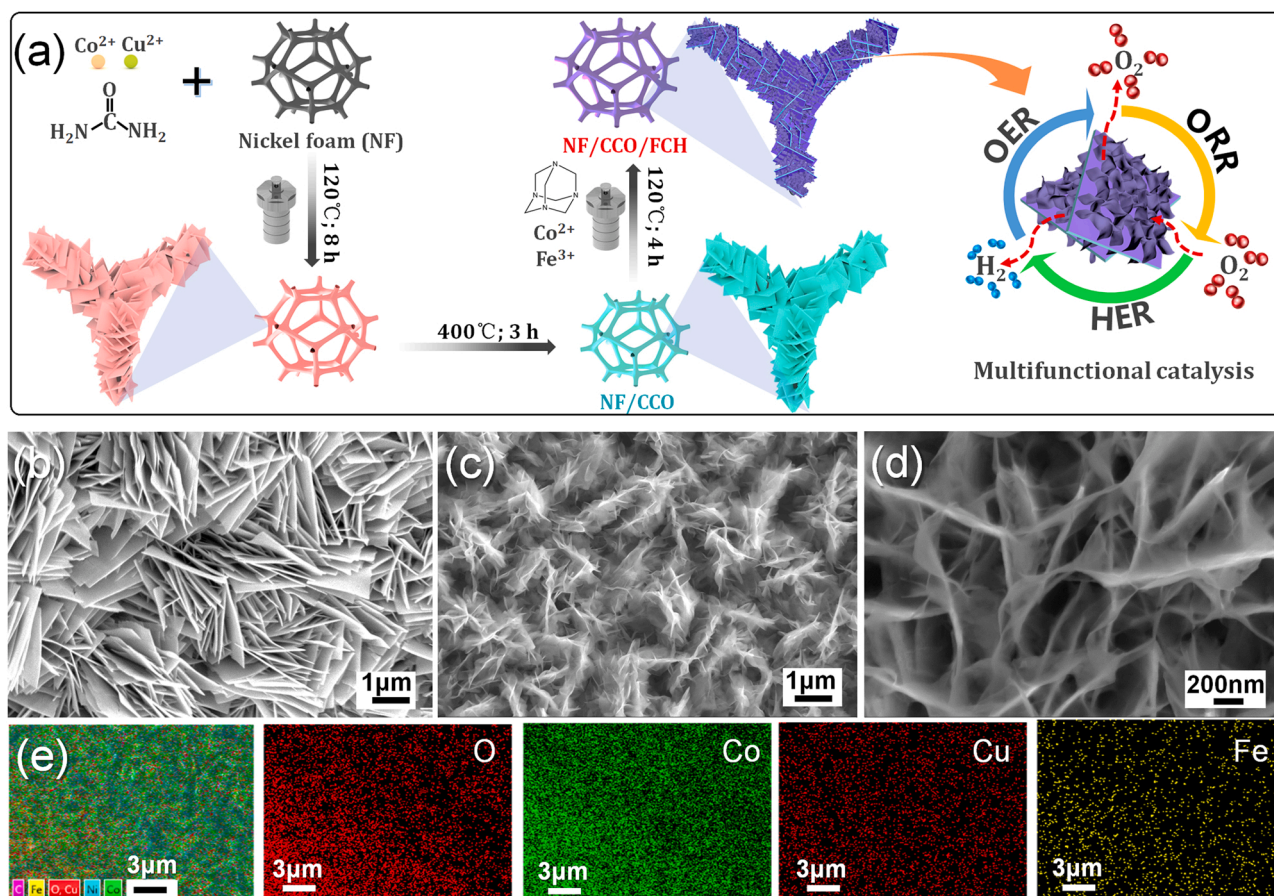


Fig. 1. (a) Schematic illustration of the fabrication procedures of the CCO-based binder-free catalysts and the multifunctional catalysis of the NF/CCO/FCH electrode toward OER, ORR and HER. SEM images of NF/CCO (b) and NF/CCO/FCH (c, d). EDS mapping images of NF/CCO/FCH (e).

spread of Co, Cu, Fe and O elements throughout the CCO/FCH nanosheets, exhibiting the atomic ratio of 4.68: 27.55: 53.10: 0.29 for Cu: Co: O: Fe via quantitative EDS analysis.

The X-ray photoelectron spectroscopy (XPS) survey spectra of CCO/FCH, CCO and FCH are shown in Fig. S10 (Supporting Information), confirming the coexistence of O, Co, Cu and Fe elements in CCO/FCH. Co 2p spectra are shown in Fig. 2f and can be fitted to two characteristic doublets accompanying with two shake-up satellites. As for CCO, the peaks centered at 779.7 eV and 794.7 eV correspond to Co^{3+} , while the peaks centered at 781.4 eV and 796.6 eV correspond to Co^{2+} , respectively. The calculated ratio of $\text{Co}^{3+}/\text{Co}^{2+}$ is 1.19, signifying that Cu doping could occupy the tetrahedral sites to increase the electron-deficient Co^{3+} content in the octahedral sites, which is profitable in terms of modulating the electronic structure of cobalt species for improved electrocatalytic OER/ORR kinetics [46]. Co 2p spectra of CCO/FCH basically shares the similar characteristic peaks with slight positive shifts (~ 0.1 eV) compared to CCO, which verifies the interfacial electronic interaction and the lowered chemical valence of cobalt in CCO/FCH with the incorporation of $\text{Co}(\text{OH})_2$. The ratio of $\text{Co}^{3+}/\text{Co}^{2+}$ is calculated to be 0.39, further proving the main oxidation state of Co (II) in FCH as expected. Fig. 2g shows the Cu 2p spectra of CCO, exhibiting four deconvolution peaks located at 933.5 and 953.4 eV that are ascribed to the two feature peaks of Cu 2p 3/2 and Cu 2p 1/2 with a spin-orbit splitting value of 19.9 eV, respectively, confirming the existence of Cu^{2+} . In comparison to CCO, it is rational that the peak intensities of Cu^{2+} in CCO/FCH have been extremely attenuated due to the evident shielding of the interlinked FCH nanosheets on the surfaces of CCO. Besides, the negative shift of 0.3–0.5 eV for the Cu^{2+} peaks further signifies the possible charge transfer between the cations due to the

intimate CCO/FCH interfaces. For the Fe 2p spectra of CCO/FCH in Fig. 2h, the peaks center at 723.1 eV and 710.9 eV are attributed to Fe^{2+} , and the rest two peaks at 713.9 eV and 725.3 eV identify the presence of Fe^{3+} , respectively. Fe^{3+} peaks exhibit larger spectral area than Fe^{2+} that reveals the distinct proportion of Fe (III) in CCO/FCH. Compared to FCH, the significant negative shifts (~ 0.4 eV) of the $\text{Fe}^{3+}/\text{Fe}^{2+}$ peaks further imply the interfacial coupling effects between CCO and FCH. O 1s spectra of the catalysts shown in Fig. 2i are deconvoluted into three peaks, where O1 peak at ca. 529 eV corresponds to the metal-oxygen bond/lattice O, while the O2 peak at 531 eV infers the defective oxygen vacancies at the surfaces of the catalysts [47]. The faded O1 and dominant proportion of O2 in CCO/FCH indicate the appreciable electronic interaction between CCO and FCH, together with abundant oxygen vacancies existing in the 2D/2D heterostructure, so as to benefit its surface electrocatalytic dynamic. The O3 peak correlates with the OH^- species and chemisorbed oxygen [48]. The raised amount of O3 in CCO/FCH evidences the M-OH (M=Co, Fe) formation that would likely to boost the OER activity associated with a set of metal-stabilized oxygen-containing intermediates (e.g., M-OOH and M-OH) [49].

3.2. HER/OER/ORR electroactivities of the heterostructure catalysts

The trifunctional catalytic properties of the self-supported catalysts were examined and compared through a standard three-electrode system. Different as-synthesized self-supported film catalysts were directly adopted as the working electrode. The onset potential shown in Fig. 3a for NF/CCO/FCH is more positive than that of NF/CCO and NF/FCH. NF/CCO/FCH displays considerable HER activity with an overpotential

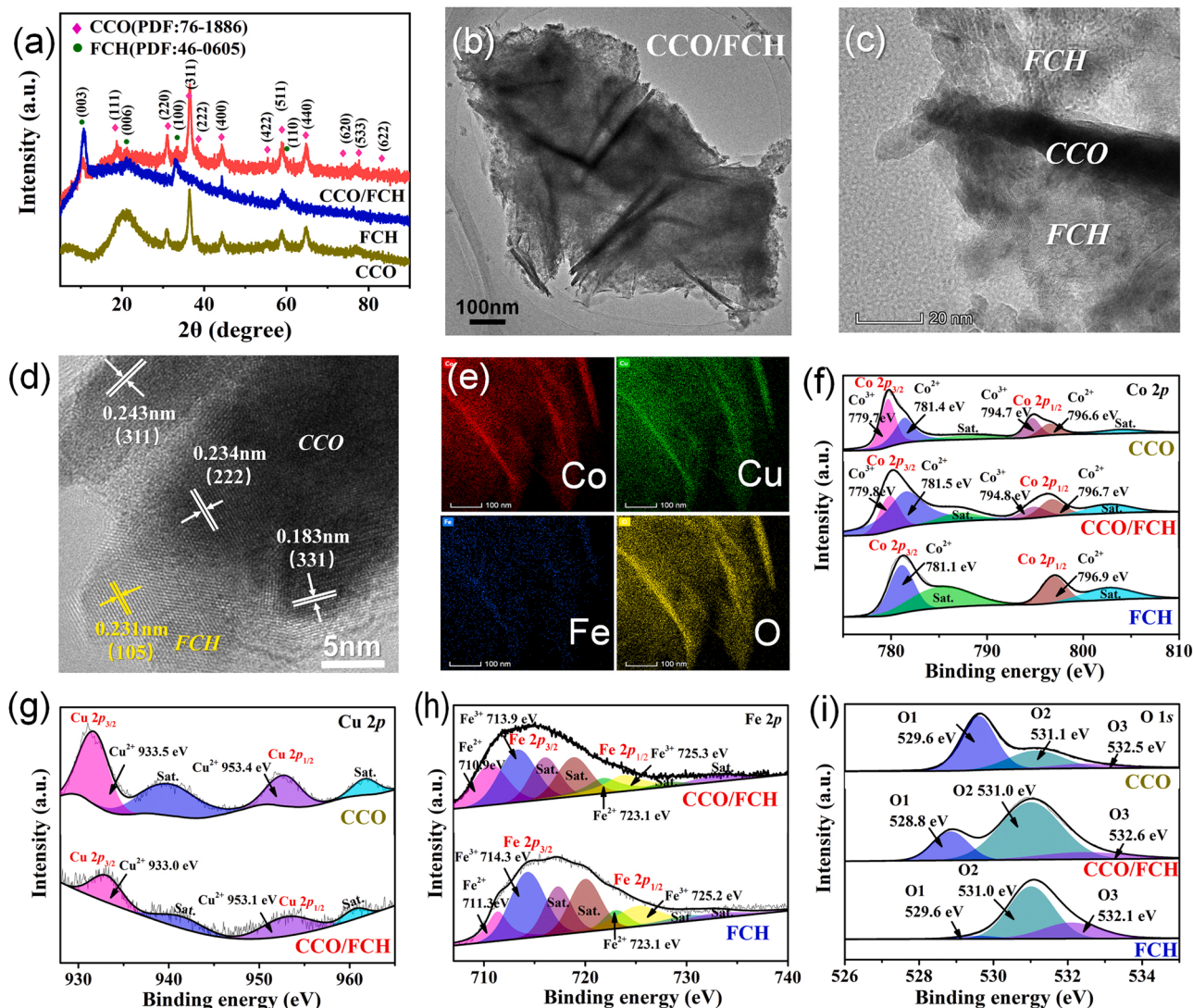


Fig. 2. (a) XRD patterns of CCO, CCO/FCH and FCH. HR-TEM images (b-d) and EDS mapping images (e) of CCO/FCH. XPS spectrum of Co 2p (f), Cu 2p (g), Fe 2p (h) and O 1s (i) for CCO, FCH and CCO/FCH, respectively.

(η) of 175 mV to reach 10 mA cm^{-2} , which is superior to NF/CCO (245 mV), NF/FCH (312 mV) and slightly inferior to the Pt/C electrode (133 mV). As demonstrated in Fig. 3b, NF/CCO/FCH gains a Tafel slope of $249.8 \text{ mV dec}^{-1}$ that outperforms NF/CCO ($252.2 \text{ mV dec}^{-1}$) and NF/FCH ($258.9 \text{ mV dec}^{-1}$), whereas is larger than that of Pt/C ($185.4 \text{ mV dec}^{-1}$), implying the decent charge transport kinetic and the good intrinsic HER activity of NF/CCO/FCH. Besides, durability plays a key role in assessing the practical potential of the catalysts. As displayed in Fig. 3c, when operated at -10 mA cm^{-2} , NF/CCO/FCH can well maintain the HER overpotential (ca. -0.21 V vs. RHE) for at least 20 h and exhibit distinctly slow decay comparable to the Pt/C benchmark. The results indicate the high catalytic activity and operational stability of the NF/CCO/FCH monolith toward the HER process.

The OER polarization curves of different electrodes are presented in Fig. 3d. NF/CCO/FCH shows a preferable OER electroactivity with a low $\eta_{j=10}$ of 257 mV, which is very close to RuO_2 and precedes NF/CCO (290 mV), Co_3O_4 (363 mV), CuO (388 mV), NF/FCH (274 mV), and NF (367 mV), respectively. Fig. 3e demonstrates the corresponding Tafel slopes. NF/CCO/FCH exhibits 94.3 mV dec^{-1} , which is the lowest among all the electrodes and manifests the faster electron-transport kinetics and superior intrinsic OER activity of NF/CCO/FCH. In addition, chronopotentiometry was adopted to characterize the working stability of NF/CCO/FCH at 10 mA cm^{-2} (Fig. 3f). NF/CCO/FCH can keep a

smaller and more stable overpotential of 260 mV upon 22 h compare to RuO_2 and NF/CCO, suggesting the outstanding stability of the binder-free NF/CCO/FCH electrode.

The LSV polarization curves of the electrodes for ORR were determined in O_2 -saturated KOH electrolyte. The onset potential for NF/CCO/FCH is close to Pt/C, and more positive compared to the other electrodes (Fig. 3g). NF/CCO/FCH produces a half-wave potential ($E_{1/2}$) of 0.83 V, which is not only comparable to Pt/C (0.85 V), but also distinctly surpasses NF/CCO (0.80 V) and other electrodes. The limited current density of NF/CCO/FCH is ca. 7.5 mA cm^{-2} at 0.4 V, much larger compared to NF/CCO, NF/FCH and Pt/C, respectively, signifying the exceptional ORR activity of NF/CCO/FCH. It is evident that CCO obtained enhanced ORR activity than Co_3O_4 , proving that atomically Cu substitution into Co_3O_4 could favor the ORR activity of the spinel $\text{Cu}_x\text{Co}_{3-x}\text{O}_4$ as expected. Compared with NF/CCO and NF/FCH, the profoundly enhanced ORR performance of NF/CCO/FCH are mainly ascribed to the synergistic effects between CCO and FCH nanosheets even though FCH itself shows inferior ORR activity. The ultrathin FCH nanosheets can not only reserve the dominantly ORR-active CCO nanosheets, but also assist to create more porous and oriented channels for oxygen diffusion and charge transfer, thus exposing more available active sites for NF/CCO/FCH during the ORR process. Besides, NF/CCO/FCH exhibits preferable ORR durability with high retention rate of the

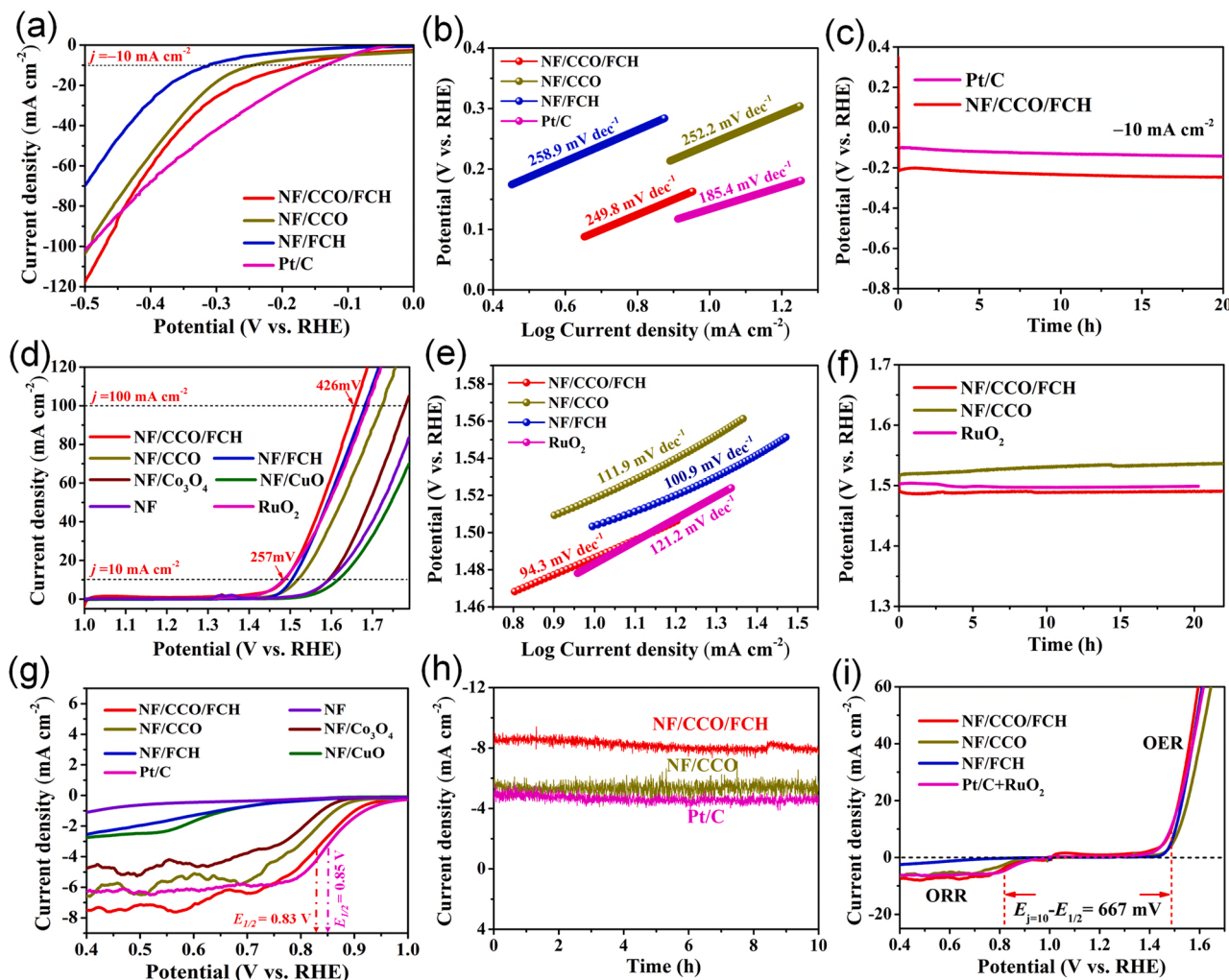


Fig. 3. Electrochemical performances of different catalysts. HER polarization curves (a) and corresponding Tafel plots (b) of NF/CCO/FCH, NF/CCO, NF/FCH, and Pt/C; (c) Chronopotentiometric measurements of NF/CCO/FCH and Pt/C at -10 mA cm^{-2} ; OER polarization curves (d) and corresponding Tafel plots (e) of different catalysts; (f) Chronopotentiometric curves of NF/CCO/FCH, NF/CCO, and RuO_2 at 10 mA cm^{-2} ; (g) ORR polarization curves of different catalyst in O_2 -saturated KOH; (h) Chronoamperometric measurements of NF/CCO/FCH, NF/CCO and Pt/C at 0.5 V (vs. RHE); (i) The overall overpotentials of NF/CCO/FCH, NF/CCO, NF/FCH, and $\text{RuO}_2 + \text{Pt/C}$ during the whole ORR and OER process.

initial current density after 10 h (Fig. 3 h). The composition and structural variation of NF/CCO/FCH after HER/OER/ORR stability tests were further investigated. As shown in the XRD patterns of Fig. S11, the characteristic peaks of the dominant CCO in NF/CCO/FCH are well preserved after 10 h for HER, OER and ORR, respectively, illuminating the structural and electrochemical endurance of the multifunctional NF/CCO/FCH catalyst.

Electrochemically active surface area (ECSA) were evaluated and obtained through the electrochemical double layer capacitances (C_{dl}) based on the cyclic voltammetry (CV) curves, occurring at the non-Faradaic region (Fig. S12a-d, Supporting Information). NF/CCO/FCH shows the highest C_{dl} value of $278.74 \text{ mF cm}^{-2}$, in comparison with NF/CCO ($182.14 \text{ mF cm}^{-2}$) and NF/FCH ($247.52 \text{ mF cm}^{-2}$). The increased C_{dl} and ECSA can be attributed to the shortened ion diffusion path and accelerated mass transfer across the interconnected ultrathin FCH nanosheets and the seamlessly contacted 2D/2D heterostructure during the oxygen catalysis process, which can improve the catalytic activity of NF/CCO/FCH with more accessible active sites [50]. The overall overpotential ($\Delta E = E_{j=10} - E_{1/2}$) of the oxygen electrode can be an indicator to evaluate the bifunctional activities. A smaller ΔE usually means better oxygen electrocatalytic performance of the electrode. As presented in Fig. 3i, NF/CCO/FCH realizes a quite low ΔE of 657 mV, which

significantly outperforms NF/CCO and can rival $\text{Pt/C} + \text{RuO}_2$, and also comparable to many recently reported high-efficiency bifunctional catalysts (Table S4), shedding light on the prominent bifunctional oxygen electroactivities of the self-supported NF/CCO/FCH monolith.

3.3. Reaction kinetic and the catalytic mechanism

The superb trifunctional electrocatalytic activities of NF/CCO/FCH are mainly contributed by following factors: (i) the conductive NF-supported catalyst with 3D opened channels and tightly grown aligned nanoarrays can establish reinforced interfaces and largely decrease the interfacial contact resistances. The merits ensure the directional electron transportation and mechanical integrity/robustness of the entire electrode during electrocatalytic process, as can be inferred from the reduced HER/OER/ORR performances of the CCO/FCH coated-NF electrode in comparison to NF/CCO/FCH (Fig. S13a-f); (ii) the CCO/FCH catalyst owns hierarchical morphology containing major mesopores from CCO and minor micropores from FCH, along with a considerable proportion of macropores created by the synergistic 2D/2D hetero-assembly, which produce a total pore volume of $0.296 \text{ cm}^3 \text{ g}^{-1}$ and a large BET specific area of $194.77 \text{ m}^2 \text{ g}^{-1}$ (Fig. S14a, b, Table S5, Supporting information). The increased active specific area and

hierarchical porosity of CCO/FCH generally favor the electrolyte accessibility and mass transport, thus promoting the HER, OER and ORR activities. (iii) the 2D/2D heterostructured CCO/FCH nanosheets are born with multiple metal electroactive sites and intimate interfaces for rapid charge transfer and expedited redox kinetics toward improved electrocatalytic performance. As demonstrated in the Nyquist plots through electrochemical impedance spectroscopy (EIS) measurements (Fig. 4a, Fig. S15, Supporting information), NF/CCO/FCH owns a smaller diameter of the semicircle, which suggests the lower charge-transfer resistances (R_{ct} : 1.80 Ω) at the catalyst/electrolyte interfaces and easier mass diffusion within the electrode, as compared to NF/CCO (R_{ct} : 2.73 Ω) and RuO₂ (R_{ct} : 5.37 Ω) for OER, or NF/CCO and Pt/C for ORR, respectively. It implies more exposed catalytic sites and available reactant pathways for the triphase interfacial redox reactions of NF/CCO/FCH. In addition, the EIS results further indicate that the superior OER/ORR bifunctionality of NF/CCO/FCH is synergistically contributed by the ORR-active CCO and OER-active FCH. (iv) the involvement of suitable Fe doping in FCH and Cu²⁺ in CCO are quite favorable for improved bifunctional oxygen catalytic activities. According to the OER/ORR polarization curves of different comparative catalysts (Fig. S16a and b, Supporting information), Cu²⁺ can mainly reduce the

ORR overpotentials, while slight Fe incorporation appreciably led to higher current densities toward OER and ORR of NF/CCO/FCH. Previous studies have also showed the positive contribution of Fe dopant for better oxygen electrochemistry. The 3d electronic structure of active Co sites in spinel oxides could rationally be modulated via site-selective Fe (II)/Fe (III) pair, thereby boosting the oxygen catalytic kinetic for more efficient active sites [48,51]. As a consequence, it is noteworthy that intact CCO nanosheets with eminent ORR activity decorating with interlinked ultrathin FCH nanosheets possessing remarkable OER activity are responsible for the superior bifunctional oxygen catalysis of the monolithic NF/CCO/FCH catalyst.

To gain more insights about the reaction kinetic and the excellent multifunctional activities of the 2D/2D heterostructured CCO/FCH catalyst, we conducted density functional theory (DFT) computations to systematically elucidate the surface energetics and the adsorption behavior of the multi-metal compound catalysts. The HER/OER/ORR catalytic pathways of NF/CCO/FCH are schemed in Fig. 4b. Configuration models of CCO, FCH and CCO/FCH used for DFT calculations are illustrated in Fig. 4c and Fig. S17-19. As for the HER process, an optimal free energy of $|\Delta G_{H^*}|$ close to zero can be a predictor for balanced H* adsorption-desorption to assess the HER activity [52]. Fig. 4e

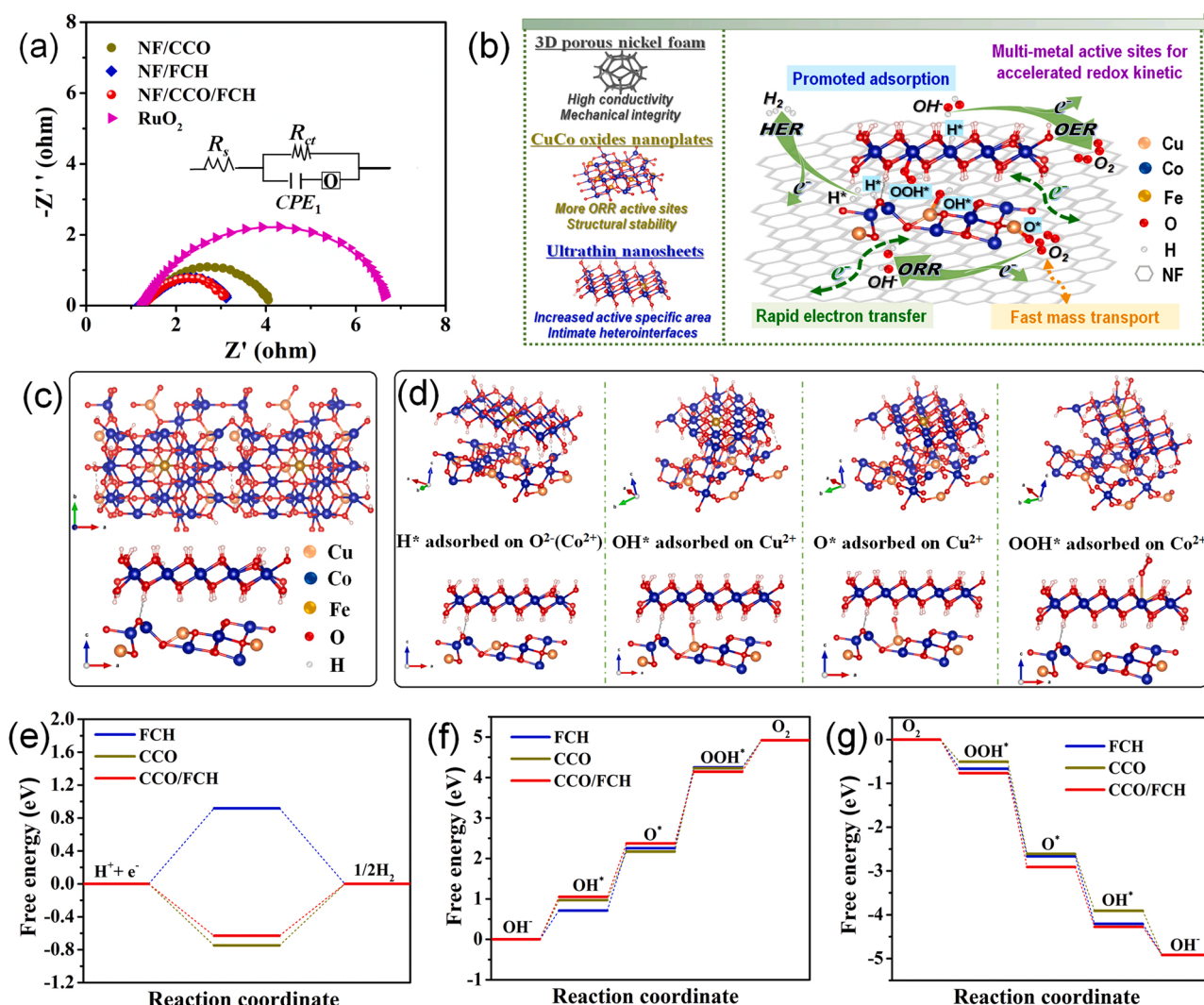
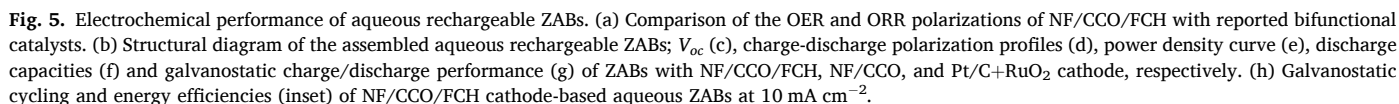


Fig. 4. (a) Nyquist plots of various electrodes for OER. Inset sketches the equivalent-circuit model for fitting, where O represents the finite layer diffusion impedance of the electrode. (b) Schematic diagram of the catalytic pathways of the trifunctional NF/CCO/FCH catalyst. (c) The configuration models (above: top-view; below: side-view) of CCO/FCH used for DFT calculations. (d) DFT-optimized configurations of the intermediates (e.g., H*, OH*, O* and OOH*) adsorbed on different dominant active center in CCO/FCH. The calculated free energy diagrams of different catalysts (FCH, CCO, CCO/FCH) for HER (e), OER (f) and ORR (g), respectively.

investigation further confirms the important role of reasonable Cu and Fe inclusion in the Co oxides (hydroxides) for enriched reactive sites and better multifunctional catalysis. All above results again uncovers the reinforced interfaces and synergistic interplay between CCO and FCH to endow CCO/FCH with multimetal active sites toward enhanced HER-/OER/ORR performance.

Given the exceptional OER/ORR bifunctionality of the NF/CCO/FCH monolith (Fig. 5a, Table S4, Supporting information), aqueous rechargeable ZABs were firstly constructed by zinc anode, the free-standing NF/CCO/FCH oxygen cathode (without using any other binders/additives and current collectors) and the alkaline electrolyte of 6 M KOH, as demonstrated in Fig. 5b. For comparison, NF/CCO and Pt/C+RuO₂ electrode were also assembled as the oxygen cathode for ZABs under the same conditions, respectively. The NF/CCO/FCH-based ZAB shows an open-circuit voltage (V_{oc}) of 1.448 V, which nearly equals that of Pt/C+RuO₂ (1.445 V) and apparently exceeds NF/CCO (1.41 V) (Fig. 5c). Fig. 5d shows the charge-discharge polarization plots. As compared to Pt/C+RuO₂ and NF/CCO counterparts, NF/CCO/FCH-based battery achieves smaller voltage gaps especially under higher current densities, consistent well with the lowered overpotentials and enhanced bifunctionality of NF/CCO/FCH discussed above. According to Fig. 5e, NF/CCO/FCH-based ZAB yields a high current density of 207.8 mA cm⁻² at 0.5 V, and a peak power density of 106.5 mW cm⁻²



at 180 mA cm^{-2} . The power output significantly exceeds NF/CCO (69.0 mW cm^{-2} at 111.7 mA cm^{-2}) and Pt/C+RuO₂ (89.3 mW cm^{-2} at 129.6 mA cm^{-2}) and is of great significance to practical applications, attributing to the attractive ORR catalytic performance of the NF/CCO/FCH cathode.

According to the galvanostatic discharge curves in Fig. 5f, the NF/CCO/FCH device exhibits a high discharge platform of 1.107 V at 10 mA cm^{-2} , superior to NF/CCO (1.04 V) and Pt/C+RuO₂ (1.09 V). In comparison with NF/CCO (796 mAh g^{-1}) and Pt/C+RuO₂-based ZAB (636 mAh g^{-1}), a higher discharge specific capacity of $808 \text{ mAh g}_{\text{Zn}}^{-1}$ (at the current density of 10 mA cm^{-2}) is delivered by the NF/CCO/FCH-based ZAB, occupying 98.5% of the theoretical specific capacity of the anodic zinc. The corresponding energy density for NF/CCO/FCH-based ZAB is determined to be $894.5 \text{ Wh kg}_{\text{Zn}}^{-1}$, which is among the high performance rechargeable ZABs and highlights NF/CCO/FCH as one of the most effective carbon-free bifunctional OER/ORR catalysts reported so far (Table S13). Notably, when the NF/CCO/FCH film was simply modified by PTFE for hydrophobic triphase interfaces and better oxygen utilization, the corresponding ZAB can still gain an impressive discharge capacity of 808 mAh g^{-1} operating with a stable discharge platform at 1.02 V , even under a high current density of 30 mA cm^{-2} (Fig. S20, Supporting Information), implying the adorable high-rate potential of NF/CCO/FCH.

The long-term cycling of ZABs are illustrated in Fig. 5g, h. Among the three, the NF/CCO/FCH based ZAB delivers the lowest voltage gap of 0.87 V at 10 mA cm^{-2} , corresponds to a round-trip efficiency of 56.2%. More impressively, the charge-discharge profiles remain almost unchanged with a slight addition of merely 0.05 V in the voltage gap even over 400 h cycling (1000 cycles), while a round-trip efficiency of 54% is acquired. In contrast, NF/CCO and Pt/C+RuO₂-based ZABs exhibit obviously larger and raised voltage gaps, along with lower energy efficiencies even within 500 cycles/200 h (Fig. S21 and S22, Supporting Information), which further prove the exceptional cyclic stability of the NF/CCO/FCH oxygen cathode. Such impressive battery performances highlight NF/CCO/FCH among the best for self-supported oxygen cathode catalysts [56,57]. XPS characterization was conducted to probe the evolution of the chemical states and the electronic structure of the cathode catalyst after battery cycling. As provided in Fig. S23a-f, the fundamental elemental components of NF/CCO/FCH can be well remained, accompanied by the co-occurrences of significant amount of zinc after 200 cycles/80 h at 10 mA cm^{-2} due to the discharge products (e.g. ZnO) attached to the surfaces of the cathode catalyst upon cycling. Compared to that in the fresh sample (Fig. 2f), the ratio of $\text{Co}^{3+}/\text{Co}^{2+}$ of cycled NF/CCO/FCH drastically raised to 1.46, revealing the reversible electrocatalytic process dominant by rich cobalt-active centers on the surfaces of the catalyst associated with the formation of the CoOOH intermediate. Moreover, after cycling at 10 mA cm^{-2} for 1000 cycles, as observed by the SEM images of NF/CCO/FCH (Fig. S24a, b, Supporting Information), the complete CCO nanosheets of the initial intersectant CCO/FCH are found to be well preserved because of high structural tolerance. While the interlinked ultrathin FCH nanosheets shrunk to nanoparticle layers spreading over the CCO nanosheets. The morphology degradation of FCH nanosheets is reasonable since the ultrathin nanosheets of transition-metal hydroxides are prone to inevitable structural change and disordered grain refinement during prolonged electrocatalytic cycles [58,59]. The result further unveils the strong interfacial bonding of the 2D/2D heterostructure against intensive charge/discharge cycling.

3.5. Electrochemical performances of flexible zinc-air batteries

With the widespread recognition of flexible/wearable electronics, FZABs are exploited as one of the most prospective flexible batteries to satisfy the expansive demand of wearable powers [60]. Endowed with the logical integration of the current collector, the active nanocatalysts and the porous gas permeation layer into “all-in-one” monolith, our

self-supported cathodes were extremely suitable for FZABs through assembling with a polished zinc foil anode and a sandwiched polymeric gel electrolyte (Fig. 6a). FZAB made from NF/CCO/FCH achieves a V_{oc} of $\sim 1.40 \text{ V}$ (Fig. S25, Supporting Information). The corresponding discharge curve in Fig. 6b gives rise to a peak power density of 35.2 mW cm^{-2} , more effective than the NF/CCO battery (Fig. S26, Supporting Information) and many previously reported transition-metal compounds and excellent bifunctional catalyst-based FZABs [37,56]. Prolonged cycling of the NF/CCO/FCH battery in Fig. 6c shows an initial round-trip efficiency of 71.6% and a small increase of 179 mV in the voltage gap after 27 h at 0.5 mA cm^{-2} , proving the admirable stability of the FZAB. As presented in Fig. 6d, once the discharge current gradually adds from 0.25 , 0.5 – 0.75 mA cm^{-2} , the FZAB can steadily discharge for 16.3 h, 14 h and 11 h, respectively, which illuminates the working durability and acceptable energy output of the flexible battery. Fig. 6e shows the rate capabilities of the FZAB under different discharge current from 0.2 to 1.8 mA cm^{-2} , in which the voltage plateau dropped from 1.34 V to 0.96 V , demonstrating an acceptable rate performance.

Conveniently, these FZABs were integrated in series or in parallel so as to satisfy the arbitrary power/energy needs of practical batteries/modules. The output voltage of two/three FZABs connected in series is 2.76 V and 4.10 V , respectively, which are twice and three times that of a single FZAB (Fig. 7a, Fig. S27a, b, Supporting Information). Demonstrated in Fig. 6f, the voltage gap for the in-series connected FZABs is nearly twice that of a single FZAB and FZABs in parallel. In addition, Nyquist plots of the FZABs through different connections were further acquired via EIS testing (Fig. S28, Supporting Information). The resistance of FZABs in series is nearly 2 times while the value of in-parallel FZABs is about half that of a single FZAB, which are in completely consistence with afore-mentioned results. The practical potential of FZABs were further evaluated. As a demonstration to power portable electronics, two FZABs were integrated in series and worn on the wrist to light up a panel consisting of 47 commercial green LEDs (Fig. 7b). The brightness of the LEDs basically remains unchanged after encountering various bending and even serious deformations (Video S1, Supporting Information), demonstrating the impressive mechanical flexibility of the batteries. Moreover, no obvious change of the charge-discharge profiles is found for the FZABs at different bending angles from 0° to 180° (Fig. 7c). The mechanical/bending stability of FZABs can be further revealed by the discharge curves upon repeated bending cycles. After 1000 bending cycles, the voltage plateau exhibits an increase of merely 27 mV as compared to the initial value of the fresh battery (Fig. 7d). The outstanding flexibility and bent stability of our FZABs confirm the mechanical robustness and effectiveness of the NF/CCO/FCH oxygen electrode.

Supplementary material related to this article can be found online at [doi:10.1016/j.apcatb.2022.122332](https://doi.org/10.1016/j.apcatb.2022.122332).

3.6. Performance of the water splitting device

To further probe the HER/OER/ORR trifunctionality of the self-supported NF/CCO/FCH catalyst/electrode and corresponding FZABs toward various practical applications, we constructed a self-powered water splitting system comprising FZABs as the power devices to drive the electrolyzer for H₂ production. Primarily, a two electrode-based alkaline water splitting cell was assembled directly utilizing a piece of NF/CCO/FCH (active area: 1.1 cm^2) as the anode and the cathode, respectively, owing to its ascendant OER and HER electrocatalytic performances. Shown in Fig. 7e, NF/CCO/FCH based two-electrode electrolyzer exhibits outstanding performance for water electrolysis with a potential of 1.51 V (1.95 V) to attain 10 mA cm^{-2} (50 mA cm^{-2}) at room temperature, which outperforms the Pt/C||RuO₂ cell (1.65 V at 10 mA cm^{-2} and 1.94 V at 50 mA cm^{-2}). Besides, prominent HER performance is demonstrated by a potential of -0.47 V to gain a high current of 100 mA cm^{-2} (Fig. S29, Supporting Information). The overall performance of NF/CCO/FCH for electrolytic water-splitting can

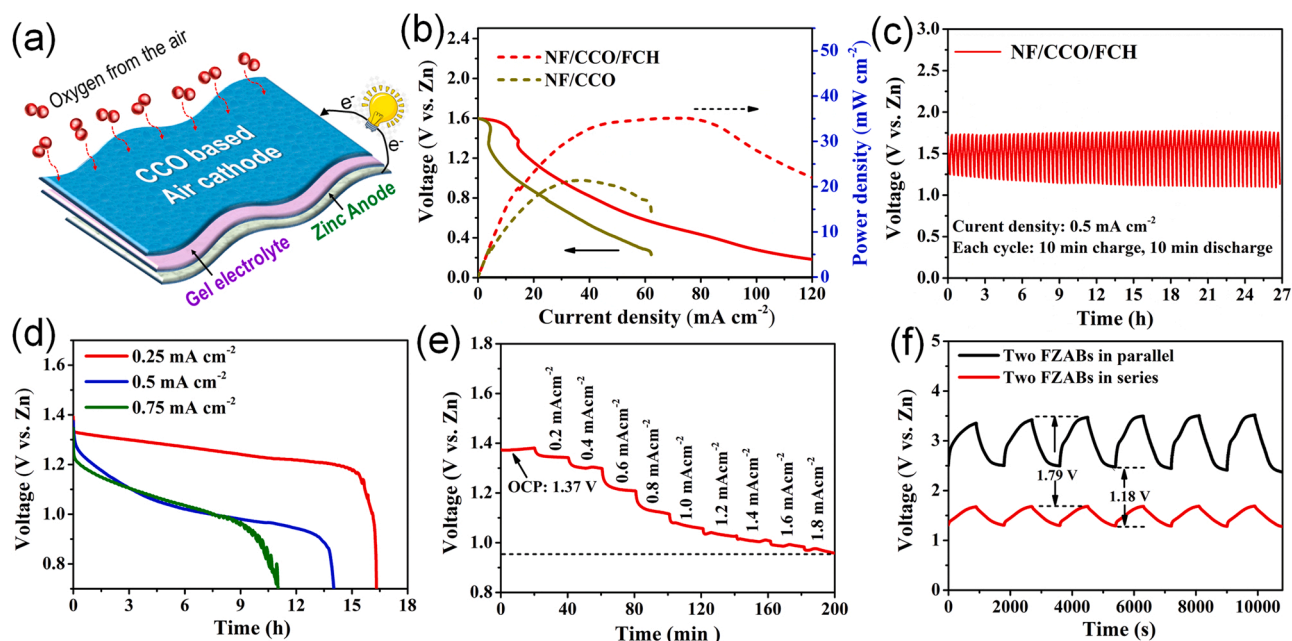


Fig. 6. Electrochemical performance of all-solid-state FZABs. (a) Structural diagram of the fabricated FZAB; (b) Discharge polarization profile and the power density curve; (c) Galvanostatic charge/discharge curves of NF/CCO/FCH-based FZAB at 0.5 mA cm^{-2} ; Discharge capacities (d) and discharge voltage curve (e) of FZAB assembled by NF/CCO/FCH cathode; (f) Galvanostatic charge/discharge curves of two FZAB connected in series or in parallel.

compete with recently reported high-efficiency trifunctional catalysts for water electrolyzers (Fig. 7f, Table S14, Supporting information) [13, 61–63]. Shown in Fig. 7g, the NF/CCO/FCH||NF/CCO/FCH electrolyzer can basically maintain its initial water splitting activity with low potentials and even larger current densities after 27 h chronopotentiometric test under 20 mA cm^{-2} . Furthermore, low potentials of ca. 1.88 V are smoothly reserved with negligible decay for the water electrolyzer even enduring intensified testing under 20, 30 and 50 for 27 h, respectively, exhibiting remarkable working stability and excellent rate performance. In order to further explore the actual potential of overall water splitting, the drainage collection method was adopted to collect H_2/O_2 produced by the self-driven water splitting device. As can be seen in Fig. 7h, once powering the electrolyzer by two in-series integrated FZABs, a large number of bubbles are rapidly generated on the surface of the anode and cathode (Video S2, Supporting Information). The amount of collected O_2 (from the anode side) and H_2 gas (from the cathode side) is calculated to be $3.13 \mu\text{mol min}^{-1}$ and $6.25 \mu\text{mol min}^{-1}$, respectively, which is in accordance with the theoretical ratio of 1: 2 (O_2 : H_2) for water splitting. Worth noting that our self-powered water splitting system with considerable hydrogen production can match and even surpass that of recently reported high-performance batteries/water splitting cells employing S- $\text{Ni}_3\text{FeN}/\text{NSG-700A}$, $\text{NiFe}/\text{NCNF}/\text{CC}$, and CoSA/N , S-HCS catalysts [54,64,65]. All above results emphasize the superiority of the self-supported trifunctional NF/CCO/FCH catalyst, and its promising use for flexible/portable power sources toward ubiquitous applications.

Supplementary material related to this article can be found online at [doi:10.1016/j.apcatb.2022.122332](https://doi.org/10.1016/j.apcatb.2022.122332).

4. Conclusion

In summary, we have designed a self-supported 2D/2D heterostructure monolith (NF/CCO/FCH) via a facile *in-situ* coupling strategy, which combines interlinked ultrathin Fe-doped cobalt hydroxides nanosheets interlacing with vertically aligned CuCo bimetal oxides nanoplates rooting on 3D porous NF scaffolds. Owing to the structural and component benefits, the robustly integrated heterostructure electrocatalyst possesses unique advantages including high conductivity,

increased active specific area, hierarchical porosity, reinforced interfaces and enriched metal reactive sites. These profitable attributes jointly favor the rapid interfacial charge transfer and mass transport, as well as expedited surface reaction kinetics of the film catalyst for promoted intrinsic HER/OER/OER activities. The developed monolithic NF/CCO/FCH can directly act as a trifunctional electrode for HER ($\eta_{j=10}$ of 175 mV), OER ($\eta_{j=10}$ of 257 mV) and ORR ($E_{1/2}$ of 0.83 V) exhibiting prominent catalytic efficiency and electrochemical durability. The superior ORR/OER bifunctionality ($\Delta E = 657 \text{ mV}$) of NF/CCO/FCH can compete with $\text{Pt}/\text{C}+\text{RuO}_2$ benchmark and rank it among the top of transition metallic compound-based bifunctional catalysts, thereby leading to high-performance rechargeable ZABs and all-solid-state FZABs. Both theoretical calculations and experimental results unravel the nature of multimetal active sites for intermediates adsorption and synergistic interplay of the 2D/2D heterostructure for accelerated catalytic kinetics. Based on the trifunctional NF/CCO/FCH electrode, a home-made water splitting cell is established that exhibits an ultralow working potential of 1.51 V upon 10 mA cm^{-2} , and a self-powered water splitting device driven by FZABs realizes high H_2 production rate. In light of the well-defined hierarchical nanoarchitecture, this 2D/2D heterostructure catalyst may broaden the general design to explore multifunctional metal-oxides nanohybrids and high-efficiency monolithic catalysts toward flexible/wearable energy storage and utilization.

CRediT authorship contribution statement

Xuhuan Yang and **Xin Cai**: Co-conceived the idea; **Zining Zhou** and **Shengsen Zhang**: Carried out materials characterizations and DFT calculation; **Xuhuan Yang**, **Yueyuan Zou**, **Jiaqi Kuang**, and **Dewei Ye**: Carried out catalyst synthesis, materials characterizations and experimental tests; **Xuhuan Yang**, **Shengsen Zhang** and **Xin Cai**: Discussed the results and co-wrote the manuscript; **Qiongzi Gao** and **Siyuan Yang**: Discussed the results, Review & Editing; **Xin Cai**: Supervision, Methodology, Co-writing & Editing the manuscript, Funding acquisition. **Yueping Fang**: Discussed the results, Funding acquisition.

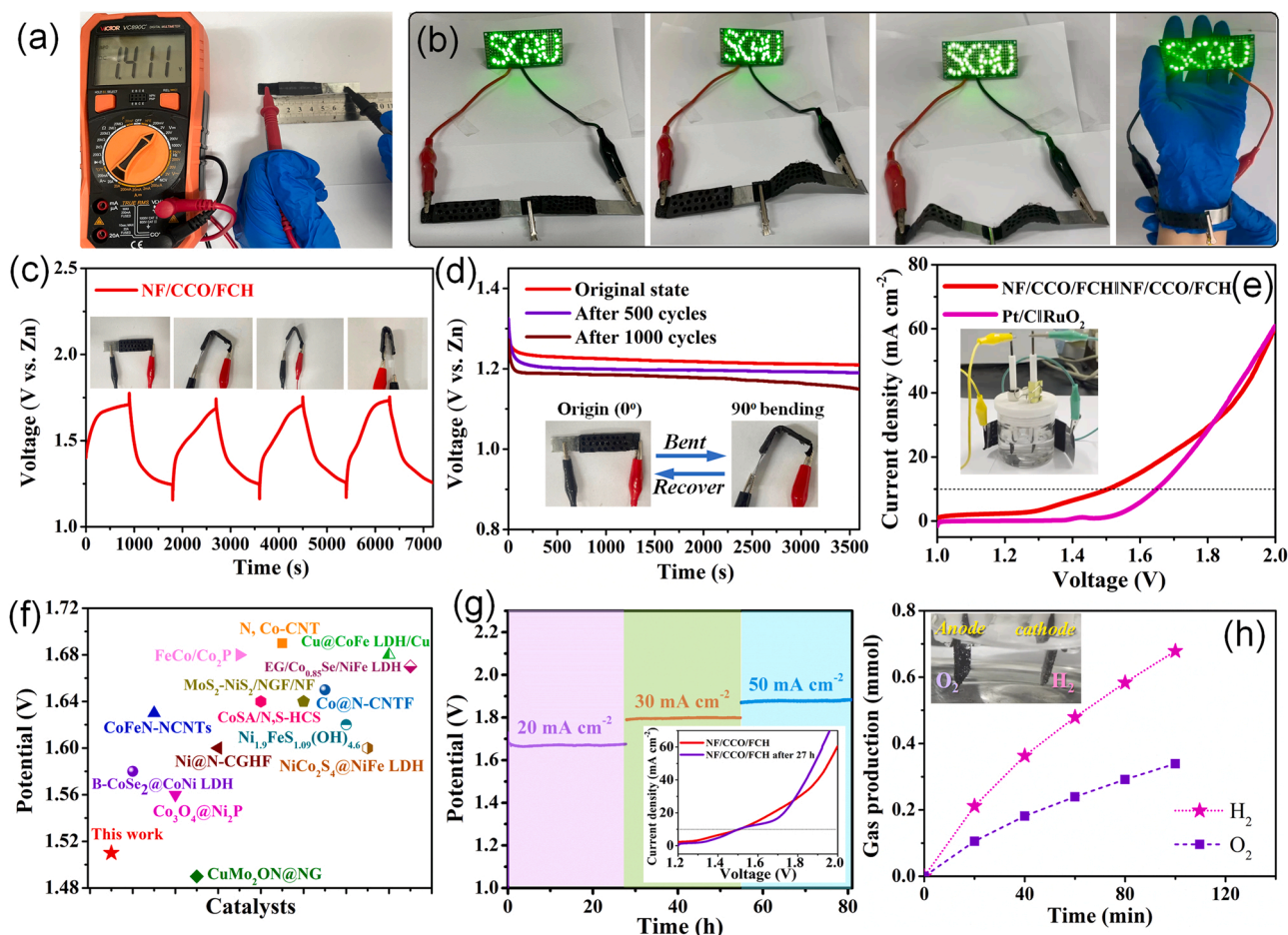


Fig. 7. (a) Optical photo of the voltage output of a single FZAB; (b) Two FZABs are connected in series to light up the "SCAU" LED panel under different bending states; (c) Galvanostatic charge/discharge curve of NF/CCO/FCH cathode-based FZABs at 0.5 mA cm^{-2} under different bending angles (0° ; 90° ; 120° and 180°); (d) Discharge voltage curves of FZAB operating at 0.5 mA cm^{-2} after different bending cycles (0, 500, 1000 cycles); (e) Polarization curves for the overall water splitting cell. Inset: optical photo of two FZABs-powered water splitting system. (f) Comparison of the potential (at 10 mA cm^{-2}) of different catalysts for water splitting. (g) Chronopotentiometric stability of the NF/CCO/FCH||NF/CCO/FCH water electrolyzer. Inset: polarization curves for the overall water splitting cell before and after 27 h testing under 20 mA cm^{-2} . (h) The gas production by the self-powered water splitting system (Inset: enlarged photo of the H_2 and O_2 generation at the surfaces of the NF/CCO/FCH cathode and the NF/CCO/FCH anode, respectively).

Declaration of Competing Interest

The authors declare that they have no known competing financial interests or personal relationships that could have appeared to influence the work reported in this paper.

Data Availability

No data was used for the research described in the article.

Acknowledgements

This research was financially supported by the Natural Science Foundation of Guangdong Province (No. 2022A1515010476), Guangxi Natural Science Foundation-Joint Funds of Guangdong and Guangxi Province (2021GXNSFDA075012), the Guangzhou Science and Technology Plan (202102020330), the National Natural Science Foundation of China (22078118).

Appendix A. Supporting information

Supplementary data associated with this article can be found in the online version at [doi:10.1016/j.apcatb.2022.122332](https://doi.org/10.1016/j.apcatb.2022.122332).

References

- [1] C.C.L. McCrory, S. Jung, I.M. Ferrer, S.M. Chatman, J.C. Peters, T.F. Jaramillo, Benchmarking hydrogen evolving reaction and oxygen evolving reaction electrocatalysts for solar water splitting devices, *J. Am. Chem. Soc.* 137 (2015) 4347–4357, <https://doi.org/10.1021/ja510442p>.
- [2] J. Fu, Z.P. Cano, M.G. Park, A. Yu, M. Fowler, Z. Chen, Electrically rechargeable zinc-air batteries: progress, challenges, and perspectives, *Adv. Mater.* 29 (2017), 1604685, <https://doi.org/10.1002/adma.201604685>.
- [3] H. Li, Q. Li, P. Wen, T.B. Williams, S. Adhikari, C. Dun, C. Lu, D. Itanze, L. Jiang, D. L. Carroll, G.L. Donati, P.M. Lundin, Y. Qiu, S.M. Geyer, Colloidal cobalt phosphide nanocrystals as trifunctional electrocatalysts for overall water splitting powered by a zinc-air battery, *Adv. Mater.* 30 (2018), 1705796, <https://doi.org/10.1002/adma.201705796>.
- [4] W. Zhao, T. Xu, T. Li, Y. Wang, H. Liu, J. Feng, S. Ding, Z. Li, M. Wu, Amorphous Iron(III)-borate nanolattices as multifunctional electrodes for self-driven overall water splitting and rechargeable zinc-air battery, *Small* 14 (2018), 1802829, <https://doi.org/10.1002/sml.201802829>.
- [5] H.F. Wang, C. Tang, B. Wang, B.Q. Li, X.Y. Cui, Q. Zhang, Defect-rich carbon fiber electrocatalysts with porous graphene skin for flexible solid-state zinc-air batteries, *Energy Storage Mater.* 15 (2018) 124–130, <https://doi.org/10.1016/j.ensm.2018.03.022>.
- [6] J. Song, Y. Chen, H. Huang, J. Wang, S.-C. Huang, Y.-F. Liao, A.E. Fetohi, F. Hu, H.-y. Chen, L. Li, X. Han, K.M. El-Khatib, S. Peng, Heterointerface engineering of hierarchically assembling layered double hydroxides on cobalt selenide as efficient trifunctional electrocatalysts for water splitting and zinc-air battery, *Adv. Sci.* 9 (2022), 2104522, <https://doi.org/10.1002/adv.202104522>.
- [7] A. Muthurasu, A.P. Tiwari, K. Chhetri, B. Dahal, H.Y. Kim, Construction of iron doped cobalt- vanadate- cobalt oxide with metal-organic framework oriented nanoflakes for portable rechargeable zinc-air batteries powered total water

- splitting, *Nano Energy* 88 (2021), 106238, <https://doi.org/10.1016/j.nanoen.2021.106238>.
- [8] X. Liu, M. Park, M.G. Kim, S. Gupta, G. Wu, J. Cho, Integrating NiCo alloys with their oxides as efficient bifunctional cathode catalysts for rechargeable zinc-air batteries, *Angew. Chem. -Int. Ed.* 54 (2015) 9654–9658, <https://doi.org/10.1002/anie.201503612>.
 - [9] Q. Shi, Q. Liu, Y. Ma, Z. Fang, Z. Liang, G. Shao, B. Tang, W. Yang, L. Qin, X. Fang, High-performance trifunctional electrocatalysts based on FeCo/Co₂P hybrid nanoparticles for zinc-air battery and self-powered overall water splitting, *Adv. Energy Mater.* 10 (2020), 1903854, <https://doi.org/10.1002/aenm.201903854>.
 - [10] Z. Qian, Y. Chen, Z. Tang, Z. Liu, X. Wang, Y. Tian, W. Gao, Hollow nanocages of NiCo_{1-x}Se for efficient zinc-air batteries and overall water splitting, *Nano Micro Lett.* 11 (2019) 28, <https://doi.org/10.1007/s40820-019-0258-0>.
 - [11] G. Zhou, G. Liu, X. Liu, Q. Yu, H. Mao, Z. Xiao, L. Wang, 1D/3D heterogeneous assembling body as trifunctional electrocatalysts enabling zinc-air battery and self-powered overall water splitting, *Adv. Funct. Mater.* 32 (2022), 2107608, <https://doi.org/10.1002/adfm.202107608>.
 - [12] H. Su, X.T. Wang, J.X. Hu, T. Ouyang, K. Xiao, Z.Q. Liu, Co-Mn spinel supported self-catalysis induced N-doped carbon nanotubes with high efficiency electron transport channels for zinc-air batteries, *J. Mater. Chem. A* 7 (2019) 22307–22313, <https://doi.org/10.1039/C9TA08064C>.
 - [13] D. Yang, W. Hou, Y. Lu, W. Zhang, Y. Chen, Cobalt phosphide nanoparticles supported within network of N-doped carbon nanotubes as a multifunctional and scalable electrocatalyst for water splitting, *J. Energy Chem.* 52 (2021) 130–138, <https://doi.org/10.1016/j.jechem.2020.04.005>.
 - [14] L.-L. Feng, G. Yu, Y. Wu, G.-D. Li, H. Li, Y. Sun, T. Asefa, W. Chen, X. Zou, High-index faceted Ni₃S₂ nanosheet arrays as highly active and ultrastable electrocatalysts for water splitting, *J. Am. Chem. Soc.* 137 (2015) 14023–14026, <https://doi.org/10.1021/jacs.5b08186>.
 - [15] H.J. Son, M.J. Kim, S.H. Ahn, Monolithic Co-N-C membrane integrating Co atoms and clusters as a self-supporting multi-functional electrode for solid-state zinc-air batteries and self-powered water splitting, *Chem. Eng. J.* 414 (2021), 128739, <https://doi.org/10.1016/j.cej.2021.128739>.
 - [16] F. Yang, T. Xiong, P. Huang, S. Zhou, Q. Tan, H. Yang, Y. Huang, M.S. Balogun, Nanostructured transition metal compounds coated 3D porous core-shell carbon fiber as monolith water splitting electrocatalysts: a general strategy, *Chem. Eng. J.* 423 (2021), 130279, <https://doi.org/10.1016/j.cej.2021.130279>.
 - [17] Z.P. Wu, H.B. Zhang, S.W. Zuo, Y. Wang, S.L. Zhang, J. Zhang, S.Q. Zang, X.W. Lou, Manipulating the local coordination and electronic structures for efficient electrocatalytic oxygen evolution, *Adv. Mater.* 33 (2021), 2103004, <https://doi.org/10.1002/adma.202103004>.
 - [18] X.T. Wang, T. Ouyang, L. Wang, J.H. Zhong, T.Y. Ma, Z.Q. Liu, Redox-Inert Fe³⁺ ions in octahedral sites of Co-Fe spinel oxides with enhanced oxygen catalytic activity for rechargeable zinc-air batteries, *Angew. Chem. Int. Ed.* 58 (2019) 13291–13296, <https://doi.org/10.1002/ange.201907595>.
 - [19] K.L. Ao, J.H. Shi, X.Y. Zhang, W.A. Daoud, Tuning oxygen vacancies in spinel nanosheets for binder-free oxygen cathodes with superior catalytic activity in zinc-air batteries, *J. Power Sources* 521 (2022), 230918, <https://doi.org/10.1016/j.jpowsour.2021.230918>.
 - [20] Y. Yang, Y. Xiong, M.E. Holtz, X. Feng, R. Zeng, G. Chen, F.J. DiSalvo, D.A. Muller, H.D. Abruna, Octahedral spinel electrocatalysts for alkaline fuel cells, *Proc. Natl. Acad. Sci. USA* 116 (2019) 24425–24432, <https://doi.org/10.1073/pnas.1906570116>.
 - [21] W.W. Liu, D. Zheng, T.Q. Deng, Q.L. Chen, C.Z. Zhu, C.J. Pei, H. Li, F.F. Wu, W. H. Shi, S.W. Yang, Y.H. Zhu, X.H. Cao, Boosting electrocatalytic activity of 3d-block metal (Hydro)oxides by ligand-induced conversion, *Angew. Chem. Int. Ed.* 60 (2021) 10614–10619, <https://doi.org/10.1002/anie.202100371>.
 - [22] Z. Zhan, X. Liang, J. Li, J. Qian, Y. Liu, S. Yang, Y. Wang, D. Gao, D. Xue, Interfacial engineering of NiO/NiCo₂O₄ porous nanofibers as efficient bifunctional catalysts for rechargeable zinc-air batteries, *ACS Appl. Mater. Interfaces* 12 (2020) 21661–21669, <https://doi.org/10.1021/acsami.0c03672>.
 - [23] X.-Z. Liu, T. Tang, W.-J. Jiang, Q.-H. Zhang, L. Gu, J.-S. Hu, Fe-doped Co₃O₄ polycrystalline nanosheets as a binder-free bifunctional cathode for robust and efficient zinc-air batteries, *Chem. Commun.* 56 (2020) 5374–5377, <https://doi.org/10.1039/D0CC01024C>.
 - [24] C. Li, X. Han, F. Cheng, Y. Hu, C. Chen, J. Chen, Phase and composition controllable synthesis of cobalt manganese spinel nanoparticles towards efficient oxygen electrocatalysis, *Nat. Commun.* 6 (2015) 7345, <https://doi.org/10.1038/ncomms8345>.
 - [25] J. Bejar, F. Espinosa-Magana, M. Guerra-Balcázar, J. Ledesma-García, L. Alvarez-Contreras, N. Arjona, L. Gerardo Arriaga, Three-dimensional-order macroporous AB₂(O₄) spinels (A, B = Co and Mn) as electrodes in Zn-air batteries, *ACS Appl. Mater. Interfaces* 12 (2020) 53760–53773, <https://doi.org/10.1021/acsami.0c14920>.
 - [26] J. Yin, Y. Li, F. Lv, Q. Fan, Y.-Q. Zhao, Q. Zhang, W. Wang, F. Cheng, P. Xi, S. Guo, NiO/CoN porous nanowires as efficient bifunctional catalysts for Zn-air batteries, *ACS Nano* 11 (2017) 2275–2283, <https://doi.org/10.1021/acsnano.7b00417>.
 - [27] X. Guo, T. Zheng, G. Ji, N. Hu, C. Xu, Y. Zhang, Core/shell design of efficient electrocatalysts based on NiCo₂O₄ nanowires and NiMn LDH nanosheets for rechargeable zinc-air batteries, *J. Mater. Chem. A* 6 (2018) 10243–10252, <https://doi.org/10.1039/C8TA02608D>.
 - [28] X.-T. Wang, T. Ouyang, L. Wang, J.-H. Zhong, Z.-Q. Liu, Surface reorganization on electrochemically-induced Zn-Ni-Co spinel oxides for enhanced oxygen electrocatalysis, *Angew. Chem. Int. Ed.* 59 (2020) 6492–6499, <https://doi.org/10.1002/ange.202006090>.
 - [29] Y. Wang, Y. Zhou, M. Han, Y. Xi, H. You, X. Hao, Z. Li, J. Zhou, D. Song, D. Wang, F. Gao, Environmentally-friendly exfoliate and active site self-assembly: thin 2D/2D heterostructure amorphous nickel-iron alloy on 2D materials for efficient oxygen evolution reaction, *Small* 15 (2019), 1805435, <https://doi.org/10.1002/sml.201805435>.
 - [30] K. Liu, H.P. Huang, Y.X. Zhu, S.P. Wang, Z.X. Lyu, X. Han, Q. Kuang, S.F. Xie, Edge-segregated ternary Pd–Pt–Ni spiral nanosheets as high-performance bifunctional oxygen redox electrocatalysts for rechargeable zinc-air batteries, *J. Mater. Chem. A* 10 (2022) 3808–3817, <https://doi.org/10.1039/D1TA10585J>.
 - [31] J. Mei, T. Liao, Z. Sun, 2D/2D heterostructures: rational design for advanced batteries and electrocatalysis, *Energy Environ. Mater.* 5 (2022) 115–132, <https://doi.org/10.1002/eeem.2.12184>.
 - [32] X. Wang, H. Li, H. Li, S. Lin, W. Ding, X. Zhu, Z. Sheng, H. Wang, X. Zhu, Y. Sun, 2D/2D 1T-MoS₂/Ti₃C₂ MXene heterostructure with excellent supercapacitor performance, *Adv. Funct. Mater.* 30 (2020), 0190302, <https://doi.org/10.1002/adfm.201910302>.
 - [33] L. An, Z. Zhang, J. Feng, F. Lv, Y. Li, R. Wang, M. Lu, R.B. Gupta, P. Xi, S. Zhang, Heterostructure-promoted oxygen electrocatalysis enables rechargeable zinc-air battery with neutral aqueous electrolyte, *J. Am. Chem. Soc.* 140 (2018) 17624–17631, <https://doi.org/10.1021/jacs.8b09805>.
 - [34] Y. Jiang, Y.-P. Deng, R. Liang, J. Fu, D. Luo, G. Liu, J. Li, Z. Zhang, Y. Hu, Z. Chen, Multidimensional ordered bifunctional air electrode enables flash reactants shuttling for high-energy flexible Zn-air batteries, *Adv. Energy Mater.* 9 (2019), 1900911, <https://doi.org/10.1002/aenm.201900911>.
 - [35] J. Wang, W. Cui, Q. Liu, Z. Xing, A.M. Asiri, X. Sun, Recent progress in cobalt-based heterogeneous catalysts for electrochemical water splitting, *Adv. Mater.* 28 (2016) 215–230, <https://doi.org/10.1002/adma.201502696>.
 - [36] Min Z, Y.L. Liu, F.P. Zhao, K.Q. Nie, N. Han, X.X. Wang, X.N. Song, J. Zhong, Y. G. Li, Metallic cobalt nanoparticles encapsulated in nitrogen-enriched graphene shells: its bifunctional electrocatalysis and application in zinc-air batteries, *Adv. Funct. Mater.* 26 (2016) 4397–4404, <https://doi.org/10.1002/adfm.201600636>.
 - [37] X. Yang, S. Li, D. Ye, J. Kuang, S. Guo, Y. Zou, X. Cai, Integrated bifunctional oxygen electrodes for flexible zinc-air batteries: from electrode designing to wearable energy storage, *Adv. Mater. Technol.* 7 (2022), 2100673, <https://doi.org/10.1002/admt.202100673>.
 - [38] C. Guan, A. Sumboja, W. Zang, Y. Qian, H. Zhang, X. Liu, Z. Liu, D. Zhao, S. J. Pennycook, J. Wang, Decorating Co/Co_x nanoparticles in nitrogen-doped carbon nanorings for flexible and rechargeable zinc-air batteries, *Energy Storage Mater.* 16 (2019) 243–250, <https://doi.org/10.1016/j.ensm.2018.06.001>.
 - [39] L. Liu, Y. Wang, F. Yan, C. Zhu, B. Geng, Y. Chen, S.-I. Chou, Cobalt-encapsulated nitrogen-doped carbon nanotube arrays for flexible zinc-air batteries, *Small Methods* 4 (2020), 1900571.
 - [40] Y. Liu, M. Pharr, G.A. Salvatore, Lab-on-skin: a review of flexible and stretchable electronics for wearable health monitoring, *ACS Nano* 11 (2017) 9614–9635, <https://doi.org/10.1002/smt.201900571>.
 - [41] L. Wan, Z. Zhao, X. Chen, P.-F. Liu, P. Wang, Z. Xu, Y. Lin, B. Wang, Controlled synthesis of bifunctional NiCo₂O₄/FeNi LDH core-shell nanoarray air electrodes for rechargeable zinc-air batteries, *ACS Sustain. Chem. Eng.* 8 (2020) 11079–11087, <https://doi.org/10.1021/acsschemeng.0c00442>.
 - [42] T. Tang, W.-J. Jiang, L.-P. Yuan, S. Niu, J.-S. Hu, L.-j. Wan, Regulating the charge diffusion of two-dimensional cobalt-iron hydroxide/graphene composites for high-rate water oxidation, *J. Mater. Chem. A* 8 (2020) 11573–11581, <https://doi.org/10.1039/D0TA03895D>.
 - [43] C. Zhu, Z. Yin, W. Lai, Y. Sun, L. Liu, X. Zhang, Y. Chen, S.-L. Chou, Fe-Ni-Mo nitride porous nanotubes for full water splitting and Zn-air batteries, *Adv. Energy Mater.* 8 (2018), 1802327, <https://doi.org/10.1002/aenm.201802327>.
 - [44] T. Ouyang, Y.-Q. Ye, C.-Y. Wu, K. Xiao, Z.-Q. Liu, Heterostructures composed of N-doped carbon nanotubes encapsulating cobalt and beta-Mo₂C nanoparticles as bifunctional electrodes for water splitting, *Angew. Chem. Int. Ed.* 58 (2019) 4923–4928, <https://doi.org/10.1002/ange.201814262>.
 - [45] W. Huang, C. Peng, J. Tang, F. Diao, M.N. Yesibolati, H. Sun, C. Engelbrekt, J. Zhang, X. Xiao, K.S. Molhave, Electronic structure modulation with ultrafine Fe₃O₄ nanoparticles on 2D Ni-based metal-organic framework layers for enhanced oxygen evolution reaction, *J. Energy Chem.* 65 (2022) 78–88, <https://doi.org/10.1016/j.jechem.2021.05.030>.
 - [46] H. Cheng, M.-L. Li, C.-Y. Su, N. Li, Z.-Q. Liu, Cu-Co bimetallic oxide quantum dot decorated nitrogen-doped carbon nanotubes: a high-efficiency bifunctional oxygen electrode for Zn-air batteries, *Adv. Funct. Mater.* 27 (2017), 1701833, <https://doi.org/10.1002/adfm.201701833>.
 - [47] X. Guo, X. Hu, D. Wu, C. Jing, W. Liu, Z. Ren, Q. Zhao, X. Jiang, C. Xu, Y. Zhang, N. Hu, Tuning the bifunctional oxygen electrocatalytic properties of core-shell Co₃O₄/NiFe LDH catalysts for Zn-air batteries: effects of interfacial cation valences, *ACS Appl. Mater. Interfaces* 11 (2019) 21506–21514, <https://doi.org/10.1021/acsami.9b04217>.
 - [48] S. Li, X. Yang, S. Yang, Q. Gao, S. Zhang, X. Yu, Y. Fang, S. Yang, X. Cai, An amorphous trimetallic (Ni-Co-Fe) hydroxide-sheathed 3D bifunctional electrode for superior oxygen evolution and high-performance cable-type flexible zinc-air batteries, *J. Mater. Chem. A* 8 (2020) 5601–5611, <https://doi.org/10.1039/D0TA00888E>.
 - [49] J. Balamurugan, T.T. Nguyen, N.H. Kim, D.H. Kim, J.H. Lee, Novel core-shell CuMo-oxynitride@N-doped graphene nanohybrid as multifunctional catalysts for rechargeable zinc-air batteries and water splitting, *Nano Energy* 85 (2021), 105987, <https://doi.org/10.1016/j.nanoen.2021.105987>.
 - [50] Y. Wang, A. Li, C. Cheng, Ultrathin Co(OH)₂ nanosheets@nitrogen-doped carbon nanoflake arrays as efficient air cathodes for rechargeable Zn-air batteries, *Small* 17 (2021), 2101720, <https://doi.org/10.1002/sml.202101720>.

- [51] Y. Liu, Y. Ying, L. Fei, Y. Liu, Q. Hu, G. Zhang, S.Y. Pang, W. Lu, C.L. Mak, X. Luo, L. Zhou, M. Wei, H. Huang, Valence engineering via selective atomic substitution on tetrahedral sites in spinel oxide for highly enhanced oxygen evolution catalysis, *J. Am. Chem. Soc.* 141 (2019) 8136–8145, <https://doi.org/10.1021/jacs.8b13701>.
- [52] J. Balamurugan, N. Thanh Tuan, D.H. Kim, N.H. Kim, J.H. Lee, 3D nickel molybdenum oxy-selenide (Ni_{1-x}MoxOSe) nanoarchitectures as advanced multifunctional catalyst for Zn-air batteries and water splitting, *Appl. Catal. B Environ.* 286 (2021), 119909, <https://doi.org/10.1016/j.apcatb.2021.119909>.
- [53] L. Yan, Y. Xu, P. Chen, S. Zhang, H. Jiang, L. Yang, Y. Wang, L. Zhang, J. Shen, X. Zhao, L. Wang, A. Freestanding, 3D heterostructure film stitched by MOF-derived carbon nanotube microsphere superstructure and reduced graphene oxide sheets: a superior multifunctional electrode for overall water splitting and Zn-air batteries, *Adv. Mater.* 32 (2020), 2003313, <https://doi.org/10.1002/adma.202003313>.
- [54] Z. Zhang, X. Zhao, S. Xi, L. Zhang, Z. Chen, Z. Zeng, M. Huang, H. Yang, B. Liu, S. J. Pennycook, P. Chen, Atomically dispersed cobalt trifunctional electrocatalysts with tailored coordination environment for flexible rechargeable Zn-air battery and self-driven water splitting, *Adv. Energy Mater.* 10 (2020), 2002896, <https://doi.org/10.1002/aenm.202002896>.
- [55] W.R. Cheng, S.B. Xi, Z.P. Wu, D.Y. Luan, X.W. Lou, In situ activation of Br-confined Ni-based metal-organic framework hollow prisms toward efficient electrochemical oxygen evolution, *Sci. Adv.* 7 (2021) eabk0919, <https://doi.org/10.1126/sciadv.abk0919>.
- [56] Y. Wang, Q. Cao, C. Guan, C. Cheng, Recent advances on self-supported arrayed bifunctional oxygen electrocatalysts for flexible solid-state Zn-air batteries, *Small* 16 (2020), 2002902, <https://doi.org/10.1002/smll.202002902>.
- [57] X.F. Lu, S.L. Zhang, E.B. Shangguan, P. Zhang, S.Y. Gao, X.W. Lou, Nitrogen-doped cobalt pyrite yolk-shell hollow spheres for long-life rechargeable Zn-air batteries, *Adv. Sci.* 7 (2020), 2001178, <https://doi.org/10.1002/advs.202001178>.
- [58] H. Chen, Z. Shen, Z. Pan, Z. Kou, X. Liu, H. Zhang, Q. Gu, C. Guan, J. Wang, Hierarchical micro-nano sheet arrays of nickel-cobalt double hydroxides for high-rate Ni-Zn batteries, *Adv. Sci.* 6 (2019), 1802002, <https://doi.org/10.1002/advs.201802002>.
- [59] W. Chen, B. Han, Y. Xie, S. Liang, H. Deng, Z. Lin, Ultrathin Co-Co LDHs nanosheets assembled vertically on MXene: 3D nanoarrays for boosted visible-light-driven CO₂ reduction, *Chem. Eng. J.* 391 (2020), 123519, <https://doi.org/10.1016/j.cej.2019.123519>.
- [60] D. Zheng, W.X. Liu, X.J. Dai, J.X. Feng, X.L. Xu, R.L. Yin, W.B. Que, W.H. Shi, F. F. Wu, H.P. Wu, X.H. Cao, Compressible Zn-air batteries based on metal-organic frameworks nanoflake-assembled carbon frameworks for portable motion and temperature monitors, *Adv. Energy Sustain. Res.* 3 (2022), 2200014, <https://doi.org/10.1002/aesr.202200014>.
- [61] Y. Zhao, J. Zhang, Y. Xie, B. Sun, J. Jiang, W.-J. Jiang, S. Xi, H.Y. Yang, K. Yan, S. Wang, X. Guo, P. Li, Z. Han, X. Lu, H. Liu, G. Wang, Constructing atomic heterometallic sites in ultrathin nickel-incorporated cobalt phosphide nanosheets via a boron-assisted strategy for highly efficient water splitting, *Nano Lett.* 21 (2021) 823–832, <https://doi.org/10.1021/acs.nanolett.0c04569>.
- [62] H. Yuan, S. Wang, Z. Ma, M. Kundu, B. Tang, J. Li, X. Wang, Oxygen vacancies engineered self-supported B doped Co₃O₄ nanowires as an efficient multifunctional catalyst for electrochemical water splitting and hydrolysis of sodium borohydride, *Chem. Eng. J.* 404 (2021), 126474, <https://doi.org/10.1016/j.cej.2020.126474>.
- [63] P.F. Guo, R.B. Wu, B. Fei, J. Liu, D. Liu, X.X. Yana, H.G. Pan, Multifunctional bayberry-like composites consisting of CoFe encapsulated by carbon nanotubes for overall water splitting and zinc-air batteries, *J. Mater. Chem. A* 9 (2021) 21741–21749, <https://doi.org/10.1039/D1TA06100C>.
- [64] C. Lai, M. Gong, Y. Zhou, J. Fang, L. Huang, Z. Deng, X. Liu, T. Zhao, R. Lin, K. Wang, K. Jiang, H. Xin, D. Wang, Sulphur modulated Ni₃FeN supported on N/S co-doped graphene boosts rechargeable/flexible Zn-air battery performance, *Appl. Catal. B Environ.* 274 (2020), 119086, <https://doi.org/10.1016/j.apcatb.2020.119086>.
- [65] C. Lai, J. Fang, X. Liu, M. Gong, T. Zhao, T. Shen, K. Wang, K. Jiang, D. Wang, In situ coupling of NiFe nanoparticles with N-doped carbon nanofibers for Zn-air batteries driven water splitting, *Appl. Catal. B Environ.* 285 (2021), 119856, <https://doi.org/10.1016/j.apcatb.2020.119856>.